

# Effect of configuration mixing on quadrupole and octupole collective states of transitional nuclei

Kosuke Nomura\*

*Department of Physics, Faculty of Science, University of Zagreb, HR-10000 Zagreb, Croatia*

(Dated: August 30, 2022)

A model is presented that simultaneously describes shape coexistence and quadrupole and octupole collective excitations within a theoretical framework based on the nuclear density functional theory and the interacting boson model. An optimal interacting-boson Hamiltonian that incorporates the configuration mixing between normal and intruder states, as well as the octupole degrees of freedom, is identified by means of self-consistent mean-field calculations using a universal energy density functional and a pairing interaction, with constraints on the triaxial quadrupole and the axially-symmetric quadrupole and octupole shape degrees of freedom. An illustrative application to the transitional nuclei  $^{72}\text{Ge}$ ,  $^{74}\text{Se}$ ,  $^{74}\text{Kr}$ , and  $^{76}\text{Kr}$  shows that the inclusion of the intruder states and the configuration mixing significantly lower the energy levels of the excited  $0^+$  states, and that the predicted low-lying positive-parity states are characterized by the strong admixture of nearly spherical, weakly deformed oblate, and strongly deformed prolate shapes. The low-lying negative-parity states are shown to be dominated by the deformed intruder configurations.

## I. INTRODUCTION

The phenomenon of shape coexistence in atomic nuclei has attracted considerable attention for many decades [1–4]. It is observed in a wide mass range in the chart of nuclides, and is often manifested by the appearance of several low-lying excited  $0^+$  states close in energy to the  $0^+$  ground state. In a spherical shell model, the emergence of the low-energy  $0^+$  levels is attributed to multiparticle-multihole intruder excitations across shell gaps. Due to the cross-shell excitations and the configuration mixing between the normal and intruder states, correlations between valence neutrons and protons are enhanced to such a degree as to sufficiently lower the  $0^+$  energies [5–10]. The observed excited  $0^+$  intruder states can be, in a mean-field picture, associated with deformations of the intrinsic nuclear shapes, as indicated by the competing minima that appear close in energy to each other in the potential energy surfaces defined in terms of the relevant shape degrees of freedom [3, 11–16].

The deformation of the ground-state shape in most medium-heavy and heavy nuclei is of reflection symmetric, quadrupole type. Additional degree of freedom that is essential to characterize the nuclear shape is the reflection asymmetric, octupole, deformation. The octupole correlations are enhanced at specific proton  $Z$  and neutron  $N$  numbers often referred to as the “octupole magic numbers,” 34, 56, 88, 134, etc., at which the coupling occurs between orbitals with opposite parities that differ by  $\Delta\ell = 3\hbar$  and  $\Delta j = 3\hbar$ , with  $\ell$  and  $j$  being, respectively, the orbital and total angular momenta of a single nucleon [17, 18]. Typical observables for the octupole collectivity are the low-lying negative-parity states, forming an approximate alternating-parity rotational band with the positive-parity yrast states, and the strong electric

dipole and octupole transitions within the band. Empirical evidence for the stable octupole shape is mostly concentrated on the axially deformed actinides [19, 20] and lanthanides [21, 22]. Related theoretical investigations have been made from various perspectives (see recent reviews, e.g., [18, 23] and references are therein).

The octupole collectivity is supposed to be present in the transitional nuclei in the mass  $A \approx 70$  and 90 regions as well, which correspond to the neutron and proton “octupole magic numbers”  $(N, Z) \approx (34, 34)$  and  $(56, 34)$ , respectively. Together with the octupole collectivity, the low-energy nuclear structure in these nuclear systems is characterized by a spectacular coexistence between prolate and oblate shapes, and a rapid structural evolution from one nucleus to another along a given isotopic chain (see, e.g., Refs. [4, 24–28], for empirical evidence). These facts make it especially attractive, and challenging, to explore the transitional nuclei in these regions.

In this paper, a model is presented that simultaneously treats the shape coexistence and the quadrupole-octupole collective excitations within a theoretical framework based on the nuclear density functional theory and the interacting boson model (IBM). Here the parameters of a version of the IBM, that is appropriate for computing spectroscopic observables characterizing the shape coexistence, as well as the octupole collective states, are determined by using the results of self-consistent mean-field (SCMF) calculations employing a universal energy density functional (EDF) [29–31]. A proof of the method is presented in an illustrative application to the nuclei  $^{72}\text{Ge}$ ,  $^{74}\text{Se}$ ,  $^{74}\text{Kr}$ , and  $^{76}\text{Kr}$ . All these are typical transitional nuclei in the neighbourhood of the neutron  $N = 40$  subshell gap and the proton “octupole magic number”  $Z = 34$ , at which both the shape coexistence and octupole correlations are expected to emerge. Note that IBM calculations including both of these effects were carried out, but on purely phenomenological grounds, to analyze the intruder and quadrupole-octupole coupled states in Cd isotopes [32–34].

---

\* [knomura@phy.hr](mailto:knomura@phy.hr)

In the following, a formalism of the configuration-mixing IBM framework that includes both the quadrupole and octupole degrees of freedom is given (Sec. II). It is then demonstrated that the parameters of the proposed boson model Hamiltonian are obtained from the SCMF calculations (Sec. III). Spectroscopic observables relevant to the shape coexistence and octupole collectivity, including the energy levels of the excited  $0^+$  states, and negative-parity states, and their transition properties, are shown in comparison with the experimental data (Sec. IV). Finally, a summary of the main results is given (Sec. V).

## II. CONFIGURATION-MIXING *sdf* IBM

The building blocks of the IBM are the monopole  $s$ , quadrupole  $d$ , and octupole  $f$  bosons, which represent, from a microscopic point of view [35, 36], spin and parity  $0^+$ ,  $2^+$ , and  $3^-$  pairs of valence nucleons, respectively. The number of bosons,  $n$ , is equal to that of the nucleon pairs, and is conserved for each nucleus.

To incorporate in the IBM system intruder states that are associated with the shell-model-like 2p-2h, 4p-4h, etc. excitations, the boson Hilbert space can be defined as the direct sum [37, 38]

$$[(sdf)^n] \oplus [(sdf)^{n+2}] \oplus [(sdf)^{n+4}] \oplus \dots, \quad (1)$$

where  $[(sdf)^{n+2k}]$  ( $k = 0, 1, 2, \dots$ ) denotes the subspace that represents the configuration of  $2k$ -particle- $2k$ -hole ( $2kp$ - $2kh$ ) excitations, comprising the  $n + 2k$   $s$ ,  $d$ , and  $f$  bosons. The basic assumption is that, like in the conventional IBM, particlelike and holelike bosons are not distinguished, hence the neighboring unperturbed subspaces  $[(sdf)^{n+2k}]$  differ in boson number by two. To avoid complication, no distinction is here made between proton and neutron bosons. In what follows, short-hand notations  $n_k \equiv n + 2k$ , and  $[n_k] \equiv [(sdf)^{n+2k}]$  are used.

The IBM Hamiltonian that is to carry out the configuration mixing of the normal  $0p$ - $0h$  and intruder states is given as

$$\hat{H} = \hat{P}_0 \hat{H}_k \hat{P}_0 + \sum_{k=1} \hat{P}_k (\hat{H}_k + \Delta_k) \hat{P}_k + \sum_{k=0} \hat{P}_{k+1} \hat{V}_{k,k+1} \hat{P}_k + (\text{H.c.}), \quad (2)$$

where  $\hat{P}_k$  represents a projection operator onto the  $2kp$ - $2kh$   $[n_k]$  configuration,  $\hat{H}_k$  the corresponding unperturbed Hamiltonian,  $\Delta_k$  the energy needed to promote  $k$  bosons across the shell closure, and  $\hat{V}_{k,k+1}$  the interaction that admixes the  $[n_k]$  with  $[n_{k+1}]$  configurations. Couplings between the configuration spaces that differ by more than two bosons are not considered, since there is no nucleon-nucleon interaction that connects such spaces.

The *sdf*-IBM Hamiltonian for each unperturbed space

is chosen to be of the form

$$\hat{H}_k = \epsilon_{d,k} \hat{n}_d + \epsilon_{f,k} \hat{n}_f + \kappa_{2,k} \hat{Q} \cdot \hat{Q} + \kappa_{3,k} \hat{O} \cdot \hat{O} + \rho_k \hat{L} \cdot \hat{L} + \eta_k \hat{\Theta}. \quad (3)$$

In the first (second) term,  $\hat{n}_d = d^\dagger \cdot \tilde{d}$  ( $\hat{n}_f = f^\dagger \cdot \tilde{f}$ ), with  $\epsilon_{d,k}$  ( $\epsilon_{f,k}$ ) representing the single  $d$  ( $f$ ) boson energy relative to the  $s$ -boson one. Note  $\tilde{d}_\mu = (-1)^\mu d_{-\mu}$  and  $\tilde{f}_\mu = (-1)^{3+\mu} f_{-\mu}$ . The third and fourth terms in (3) stand for quadrupole-quadrupole and octupole-octupole interactions, respectively. The quadrupole  $\hat{Q}$  and octupole  $\hat{O}$  operators read

$$\hat{Q} = s^\dagger \tilde{d} + d^\dagger s + \chi_k (d^\dagger \times \tilde{d})^{(2)} + \chi'_k (f^\dagger \times \tilde{f})^{(2)}, \quad (4)$$

$$\hat{O} = s^\dagger \tilde{f} + f^\dagger s + \chi''_k (d^\dagger \times \tilde{f} + f^\dagger \times \tilde{d})^{(3)}, \quad (5)$$

with  $\chi_k$ ,  $\chi'_k$ , and  $\chi''_k$  dimensionless parameters. The last two terms in (3),  $\hat{L} \cdot \hat{L}$  and  $\hat{\Theta}$ , are here introduced to describe quantitative details of energy spectra. The term  $\hat{L} \cdot \hat{L}$ , with  $\hat{L}$  the boson angular momentum operator  $\hat{L} = \sqrt{10}(d^\dagger \times \tilde{d})^{(1)}$ , plays a role to describe deformed rotors, and is specifically considered for the well deformed configurations. The term  $\hat{\Theta}$  denotes a three-body boson term of the form

$$\hat{\Theta} = \sum_{\lambda} ((d^\dagger \times d^\dagger)^{(\lambda)} \times d^\dagger)^{(3)} \cdot ((\tilde{d} \times \tilde{d})^{(\lambda)} \times \tilde{d})^{(3)}, \quad (6)$$

and is particularly needed to describe the quasi- $\gamma$  band of  $\gamma$  soft nuclei [39–42]. Note also that the Hamiltonian  $\hat{H}_k$  contains two-body  $f$ -boson interactions in the  $\hat{Q} \cdot \hat{Q}$  and  $\hat{O} \cdot \hat{O}$  terms. This is to account for some observed nonyrast states that require more than one  $f$  boson in the model space, e.g., those of double-octupole phonon nature.  $\kappa_{2,k}$ ,  $\kappa_{3,k}$ ,  $\rho_k$ , and  $\eta_k$  are interaction strengths. The mixing interaction  $\hat{V}_{k,k+1}$  in (2) reads

$$\hat{V}_{k,k+1} = \omega_{s,k} (s^\dagger \cdot s^\dagger) + \omega_{d,k} (d^\dagger \cdot d^\dagger) + \omega_{f,k} (f^\dagger \cdot f^\dagger) + (\text{H.c.}), \quad (7)$$

with  $\omega_{s,k}$ ,  $\omega_{d,k}$ , and  $\omega_{f,k}$  the strength parameters.

The geometric structure of the IBM is analyzed by means of the coherent state introduced in Refs. [43–45]. In a similar fashion to Eq. (1), the coherent state for the configuration mixing IBM,  $|\Psi\rangle$ , is given as a direct sum [46]

$$|\Psi\rangle = |\Psi_0(\vec{\alpha}_0)\rangle \oplus |\Psi_1(\vec{\alpha}_1)\rangle \oplus |\Psi_2(\vec{\alpha}_2)\rangle \oplus \dots \quad (8)$$

$|\Psi_k(\vec{\alpha}_k)\rangle$  stands for the coherent state for each unperturbed  $[n_k]$  boson subspace, and is defined, up to the normalization factor, as

$$|\Psi_k(\vec{\alpha}_k)\rangle \propto \left( s^\dagger + \sum_{\mu} \alpha_{2\mu}^{(k)} d_{\mu}^{\dagger} + \sum_{\mu} \alpha_{3\mu}^{(k)} f_{\mu}^{\dagger} \right)^{n_k} |0\rangle. \quad (9)$$

The ket  $|0\rangle$  denotes the boson vacuum, i.e., the inert core. Real coefficients  $\vec{\alpha}_k \equiv (\alpha_{2\mu}^{(k)}, \alpha_{3\mu}^{(k)})$  represent amplitudes

analogous to the collective variables in the geometrical model [47]. Specifically,

$$\alpha_{20}^{(k)} = \beta_{2,k} \cos \gamma_k, \quad \alpha_{2\pm 1}^{(k)} = 0, \quad \alpha_{2\pm 2}^{(k)} = \frac{1}{\sqrt{2}} \beta_{2,k} \sin \gamma_k, \quad (10)$$

while, for the octupole modes, only the axially symmetric deformation is assumed to be relevant, i.e.,

$$\alpha_{3\mu}^{(k)} = \beta_{3,k} \delta_{\mu,0}. \quad (11)$$

It is further assumed that the amplitudes  $\beta_{2,k}$  and  $\beta_{3,k}$  are proportional to the axial quadrupole and octupole deformations in the geometrical model, i.e.,

$$\beta_{2,k} \equiv C_{2,k} \beta_2, \quad \beta_{3,k} \equiv C_{3,k} \beta_3, \quad (12)$$

with constants of proportionality  $C_{2,k}$  and  $C_{3,k}$  defined separately for the unperturbed spaces, and that the triaxiality  $\gamma_k$  in the boson system is identical to the fermionic counterpart,  $\gamma$ , and is common for all the unperturbed spaces, i.e.,  $\gamma_k = \gamma$ .

The potential energy surface for the boson system is defined in terms of the three deformation variables  $\beta_2$ ,  $\gamma$ , and  $\beta_3$ , and is calculated as the expectation value of the Hamiltonian (2) in the coherent state of (8). The energy surface is actually obtained in the form of a  $(k+1) \times (k+1)$  matrix  $\mathbf{E}(\beta_2, \gamma, \beta_3)$ . The diagonal element of the matrix is calculated as

$$E_{k,k}(\beta_2, \gamma, \beta_3) = \langle \Psi_k(\vec{\alpha}_k) | \hat{H}_k | \Psi_k(\vec{\alpha}_k) \rangle + \Delta_k, \quad (13)$$

where  $\Delta_k$  enters only for  $k \geq 1$ , while the nondiagonal part

$$E_{k,k+1}(\beta_2, \gamma, \beta_3) = E_{k+1,k}(\beta_2, \gamma, \beta_3) = \langle \Psi_{k+1}(\vec{\alpha}_{k+1}) | \hat{V}_{k,k+1} | \Psi_k(\vec{\alpha}_k) \rangle. \quad (14)$$

Explicit analytical forms of the quantities (13) and (14) are given in the Appendix A. As in the literature [46, 48], the lowest-energy eigenvalue of the coherent-state matrix  $\mathbf{E}(\beta_2, \gamma, \beta_3)$  at each set of the coordinates  $(\beta_2, \gamma, \beta_3)$  is here taken as the energy surface for the boson system.

The bosonic energy surface depends on the parameters of the Hamiltonian, and on the constants of proportionality  $C_{2,k}$  and  $C_{3,k}$  (12). For each  $[n_k]$  configuration, there are nine parameters in the unperturbed Hamiltonian  $\hat{H}_k$ , the proportionality parameters  $C_{2,k}$  and  $C_{3,k}$  (12), and the energy offset  $\Delta_k$  ( $k \geq 1$ ). In addition, the mixing interaction  $\hat{V}_{k,k+1}$ , connecting the subspaces  $[n_k]$  and  $[n_{k+1}]$ , has three parameters for each  $k$  [see Eq. (7)]. These parameters are determined by the procedure described below.

### III. PROCEDURE TO BUILD THE IBM HAMILTONIAN

In the first step, for each nucleus, the constrained SCMF calculations [49] are carried out within the framework of the relativistic Hartree-Bogoliubov method [30,

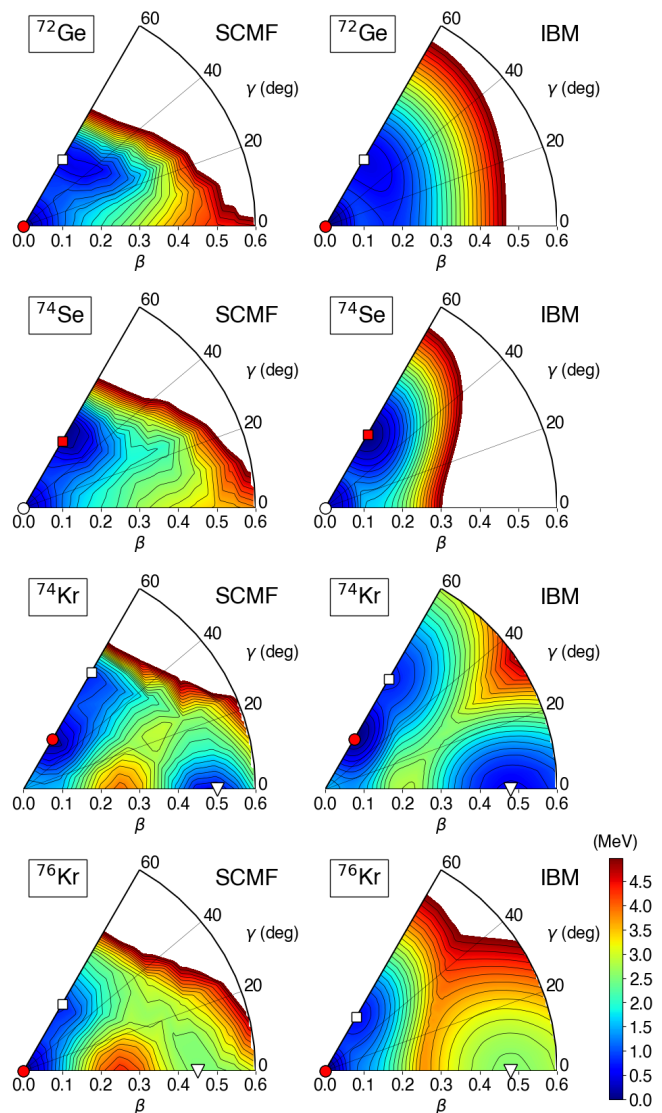


FIG. 1. Left column: Triaxial quadrupole SCMF potential energy surfaces for the  $^{72}\text{Ge}$ ,  $^{74}\text{Se}$ ,  $^{74}\text{Kr}$ , and  $^{76}\text{Kr}$  isotopes as functions of the  $\beta_2$  and  $\gamma$  deformations, computed by the constrained relativistic Hartree-Bogoliubov method with the density-dependent point-coupling interaction and the separable pairing force of finite range. Right column: Corresponding energy surfaces for the boson system. The energy difference between neighboring contours is 0.2 MeV. The minima associated with the 0p-0h, 2p-2h, and 4p-4h unperturbed configurations are identified by the circle, square, and triangle, respectively, and the solid symbol with color red denotes the global minimum.

[50, 51] using the density-dependent point-coupling interaction [52] and the separable pairing force of finite range [53]. Two sets of the SCMF calculations are performed, with constraints on the (i) triaxial quadrupole  $Q_{20}$  and  $Q_{22}$  and on the (ii) axial quadrupole  $Q_{20}$  and octupole  $Q_{30}$  moments.

The SCMF calculations provide potential energy sur-

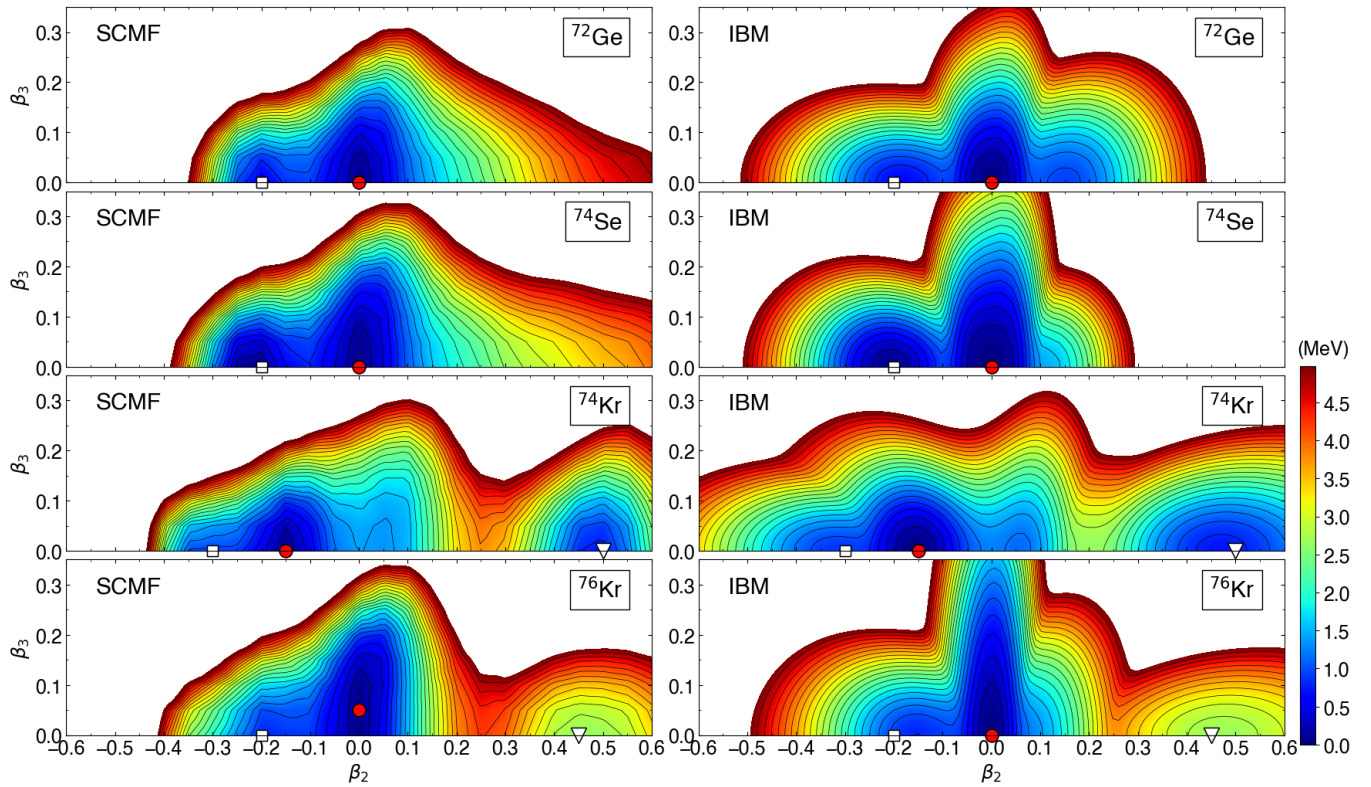


FIG. 2. Same as Fig. 1, but for the axially symmetric quadrupole and octupole SCMF and IBM potential energy surfaces as functions of the  $\beta_2$  and  $\beta_3$  deformations.

faces as functions of the triaxial quadrupole ( $\beta_2$ - $\gamma$ ) and axially symmetric quadrupole-octupole ( $\beta_2$ - $\beta_3$ ) deformations, which are shown in the first columns of Figs. 1 and 2, respectively. Here, the  $\beta_2$ ,  $\gamma$ , and  $\beta_3$  deformations can be obtained through the relations

$$\beta_2 = \frac{\sqrt{5\pi}}{3AR_0^2} \sqrt{\langle \hat{Q}_{20} \rangle^2 + 2\langle \hat{Q}_{22} \rangle^2}, \quad (15)$$

$$\gamma = \arctan \sqrt{2} \frac{\langle \hat{Q}_{22} \rangle}{\langle \hat{Q}_{20} \rangle}, \quad (16)$$

$$\beta_3 = \frac{\sqrt{7\pi}}{3AR_0^3} \langle \hat{Q}_{30} \rangle, \quad (17)$$

with  $R_0 = 1.2A^{1/3}$  fm.

One finds, in the SCMF  $\beta_2$ - $\gamma$  energy surfaces for  $^{72}\text{Ge}$  and  $^{74}\text{Se}$  (Fig. 1), two minima that are close in energy to each other, one spherical and the other oblate. For  $^{74}\text{Kr}$  ( $^{76}\text{Kr}$ ), in addition to two oblate (a spherical and an oblate) minima, a third, strongly prolate deformed minimum appears at the deformation  $\beta_2 = 0.5$  (0.45). The prolate minimum in  $^{74}\text{Kr}$  is deeper in energy than the one for  $^{76}\text{Kr}$ , and is even close to the oblate global minimum.

The  $\beta_2$ - $\beta_3$  SCMF energy surfaces, shown in Fig. 2, exhibit  $\beta_3$  softness in  $^{74}\text{Se}$  and  $^{76}\text{Kr}$ . The former nucleus is predicted to be soft in the  $\beta_2$  deformation as well.

The softness implies sizable correlations arising from the shape mixing, which play an important role in the spectroscopic properties. For  $^{74}\text{Se}$ , the global minimum in the  $\beta_2$ - $\beta_3$  deformation plane occurs at the spherical configuration, while in the  $\beta_2$ - $\gamma$  plane the oblate global minimum is obtained. The discrepancy is due to the fact that the constrained SCMF calculations are here performed separately within the  $\beta_2$ - $\gamma$  and  $\beta_2$ - $\beta_3$  deformation spaces. However, the energy difference between the two minima is negligibly small on both the  $\beta_2$ - $\gamma$  and  $\beta_2$ - $\beta_3$  surfaces, i.e., the spherical local (global) minimum in the  $\beta_2$ - $\gamma$  ( $\beta_2$ - $\beta_3$ ) energy surface of  $^{74}\text{Se}$  is only 72 (29) keV above (below) the oblate global (local) minimum. Such a difference would not affect much the resulting spectroscopic properties.

The SCMF results are subsequently used as microscopic inputs to build the configuration-mixing *sdf*-IBM Hamiltonian (2). This procedure consists of a fermion-to-boson mapping developed in Refs. [54, 55]: The potential energy surface, computed by the constrained SCMF method for each nucleus, is mapped onto the expectation value of the IBM Hamiltonian in the boson coherent state, and this mapping procedure specifies the strength parameters of the IBM Hamiltonian. In other words, the IBM parameters are calibrated so that the SCMF and IBM energy surfaces are similar in topology to each other. The mapping procedure has been extended further

so as to include in the usual boson space the configuration mixing between normal and intruder states [56], and octupole degrees of freedom [57].

For the considered nuclei, the neutron  $N = 28-50$  and proton  $Z = 28-50$  major shells are taken as the normal configuration space. The intruder states are here assumed to be the proton excitations across the  $Z = 28$  major shell. The two configurations,  $[n_0]$  and  $[n_1]$ , are considered for  $^{72}\text{Ge}$  and  $^{74}\text{Se}$ , since the SCMF potential energy surfaces show two minima (see Figs. 1 and 2). On the other hand, since there appears an additional prolate third minimum for  $^{74}\text{Kr}$  and  $^{76}\text{Kr}$ , the three configurations,  $[n_0]$ ,  $[n_1]$ , and  $[n_2]$ , are included in the boson spaces for these nuclei. According to the prescription proposed in Ref. [56], the unperturbed Hamiltonians  $\hat{H}_k$  for the 0p-0h, 2p-2h, and 4p-4h configurations are associated with those minima on the SCMF  $\beta_2$ - $\gamma$  energy surface that correspond to the smallest, second larger, and third larger  $\beta_2$  deformations, respectively. The correspondence between the  $[n_k]$ -boson configuration and the mean-field minimum is indicated in the SCMF energy surfaces in Figs. 1 and 2.

Since the full Hamiltonian (2) contains a large number of parameters, it is plausible to consider each sector of the Hamiltonian separately in the following way.

1. First, the  $sd$ -boson sector of each unperturbed Hamiltonian  $\hat{H}_k$  is fixed. The relevant parameters,  $\epsilon_{d,k}$ ,  $\kappa_{2,k}$ ,  $\chi_k$ ,  $\eta_k$ , and  $C_{2,k}$ , are then chosen so that the topology of the  $\beta_2$ - $\gamma$  SCMF energy surface in the vicinity of the corresponding minimum is reproduced by the diagonal matrix element  $E_{k,k}(\beta_2, \gamma, 0)$  (13), i.e., the expectation value of the unperturbed Hamiltonian in the  $[n_k]$  space.
2. The parameter for the  $\hat{L} \cdot \hat{L}$  term,  $\rho_k$ , is derived separately from those described above, in such a way [58] that the cranking moment of inertia calculated at each mean-field minimum in the intrinsic frame of the boson system [59], is equal to the Inglis-Belyaev [60, 61] moment of inertia,  $\mathcal{I}_{\text{IB}}$ , computed by the same constrained SCMF method. This term is here taken into account in those well-deformed configurations for which the Inglis-Belyaev values are calculated to be  $\mathcal{I}_{\text{IB}} > 10 \text{ MeV}^{-1}$ , specifically, the 2p-2h and 4p-4h configurations for  $^{74}\text{Kr}$ , and the 4p-4h configuration for  $^{76}\text{Kr}$ . It is also noted that the Inglis-Belyaev moments of inertia are here increased by 30 %. This is to take into account the fact that the Inglis-Belyaev formula gives the moments of inertia that are by typically 30-40 % smaller than the empirical ones.
3. The mixing interaction  $\hat{V}_{k,k+1}$  is introduced. Here, the strengths  $\omega_{s,k}$ ,  $\omega_{d,k}$ , and  $\omega_{f,k}$  are assumed to be equal to each other for each  $k$ , i.e.,  $\omega_{f,k} = \omega_{d,k} = \omega_{s,k} \equiv \omega_k$ . The energy offset  $\Delta_k$ , and the parameter  $\omega_k$  for  $\hat{V}_{k,k+1}$  are obtained so that the energy

difference between the neighboring mean-field minima corresponding to the  $[n_k]$  and  $[n_{k+1}]$  configurations, and the topology of the barrier separating the two minima, respectively, are reproduced by the lowest-energy eigenvalue of the matrix  $\mathbf{E}(\beta_2, \gamma, 0)$ .

4. Finally, the  $f$ -boson sector of the Hamiltonian (3) is fixed. The relevant parameters,  $\epsilon_{f,k}$ ,  $\chi'_k$ ,  $\kappa_{3,k}$ ,  $\chi''_k$ , and  $C_{3,k}$ , are determined so that the diagonal matrix element for the  $[n_k]$  subspace,  $E_{k,k}(\beta_2, 0^\circ, \beta_3)$ , should reproduce the topology of the SCMF  $\beta_2$ - $\beta_3$  energy surface in the vicinity of the corresponding minimum. In this step, the parameters for the  $sd$ -boson sector of the Hamiltonian, mixing strength  $\omega_k$ , and the offset energy  $\Delta_k$ , obtained in the previous three steps, are kept unchanged.

Table I lists the adopted parameters for the studied nuclei.

The  $\beta_2$ - $\gamma$  and  $\beta_2$ - $\beta_3$  mapped-IBM energy surfaces are shown in the right columns of Figs. 1 and 2, respectively. They are similar in topology to the original SCMF energy surfaces up to a few MeV excitation from the global minimum. There are, however, some discrepancies as well. In particular, the SCMF  $\beta_2$ - $\beta_3$  energy surface for  $^{76}\text{Kr}$  shows the global minimum at  $\beta_3 \approx 0.05 \neq 0$ . The nonzero  $\beta_3$  minimum is not reproduced in the bosonic one, which rather gives the minimum at  $\beta_3 = 0$ . Note, however, that the SCMF energy surface is also considerably soft along the  $\beta_3$  direction. Indeed the global minimum at  $(\beta_2, \beta_3) \approx (0.0, 0.05)$  is by only 17 keV lower in energy than that configuration on the  $\beta_3 = 0$  axis with the same  $\beta_2$ , i.e.,  $(\beta_2, \beta_3) \approx (0.0, 0.0)$ . The energy difference is so small that it would not have much influence on the final results.

Another discrepancy is that the  $\beta_2$ - $\gamma$  SCMF energy surfaces for  $^{72}\text{Ge}$  and  $^{74}\text{Se}$  are flat on the prolate side, extending to the region corresponding to large  $\beta_2$  deformation, while the bosonic surfaces are more rigid in  $\gamma$  deformation. This is partly because the analytical form of the IBM energy surface has too limited degrees of freedom to reproduce such a topology. However, the mean-field configurations most relevant to the low-lying collective states are those in the vicinity of each minimum, hence the mapping is carried out primarily to reproduce the topology around the minimum.

#### IV. RESULTS FOR THE SPECTROSCOPIC PROPERTIES

With all the parameters determined by the procedure described in the previous section, the Hamiltonian (2) is diagonalized within the boson Hilbert space defined in Eq. (1), producing spectroscopic observables. For the diagonalization, the boson  $m$ -scheme basis is used.

In order to reduce computational time, a truncation is made so that the maximum number of  $f$  bosons is limited as  $n_f^{\text{max}} = 3$ . The truncation makes sense, particularly

TABLE I. Adopted parameters for the configuration-mixing *sdf*-IBM Hamiltonian. See Eqs. (3) and (7), and (12) for definitions.

	Config.	$n_k$	$\epsilon_{d,k}$ (MeV)	$\kappa_{2,k}$ (keV)	$\chi_k$	$\chi'_k$	$\rho_k$ (keV)	$\eta_k$ (keV)	$\epsilon_{f,k}$ (MeV)	$\kappa_{3,k}$ (keV)	$\chi''_k$	$C_{2,k}$	$C_{3,k}$	$\omega_k$ (keV)	$\Delta_k$ (MeV)
$^{72}\text{Ge}$	0p-0h	7	1.9	-85	0.15	-0.15	0	0	-2.0	35	-0.8	6.5	1.9		
	2p-2h	9	1.05	-70	0.20	-0.50	0	55	-2.2	28	-1.6	2.8	2.4	40	1.4
$^{74}\text{Se}$	0p-0h	8	1.9	-85	0.15	0.15	0	0	-2.0	35	-0.8	6.5	1.4		
	2p-2h	10	1.2	-70	0.67	-0.70	0	50	-2.2	28	-1.4	3.2	2.4	35	1.9
$^{74}\text{Kr}$	0p-0h	9	1.0	-57	0.95	0.95	0	0	-2.0	25	-1.6	4.5	2.0		
	2p-2h	11	0.81	-56	0.65	0.65	6.4	0	-2.0	24	-1.4	2.3	2.4	40	2.3
	4p-4h	13	0.48	-42	-0.90	-0.36	12	0	-2.0	23	-1.8	2.0	2.6	30	4.7
$^{76}\text{Kr}$	0p-0h	9	1.9	-36	0.67	0.67	0	0	-2.0	22	-0.8	6.0	0.9		
	2p-2h	11	0.85	-33	0.75	0.75	0	0	-2.0	22	-1.8	3.6	2.2	40	1.3
	4p-4h	13	0.42	-35	-0.60	-0.60	22	0	-2.1	20	-2.0	1.7	2.6	30	5.6

because the majority of the low-energy states with positive and negative parity turn out to be essentially of zero- and one-*f*-boson characters, respectively. Sensitivity of the calculated observables to this truncation will be discussed in detail in Sec. IV D.

#### A. Effect of configuration mixing

A drastic, as well as favorable, effect of including the configuration mixing in the *sdf*-IBM is the lowering of the excited  $0^+$  states. Figure 3 compares between the low-energy spectra calculated within the *sdf*-IBM including and excluding the configuration mixing. In the latter calculation, only a single configuration corresponding to the  $[n_0]$  normal space is considered, and the Hamiltonian  $\hat{H}_0$  is associated with the global minimum.

By the inclusion of the configuration mixing, the  $0_2^+$  and  $0_3^+$  energy levels are significantly lowered in all the four nuclei considered. Another non-yrast level,  $2_2^+$ , is also lowered in the mixing calculation. The positive-parity yrast states,  $2_1^+$  and  $4_1^+$ , remain unchanged for  $^{72}\text{Ge}$  and  $^{74}\text{Se}$ , but are lowered for  $^{74}\text{Kr}$  and  $^{76}\text{Kr}$  by the mixing. The configuration mixing also has impacts on the negative-parity levels. The *sdf*-IBM calculation with only a single configuration generally gives an approximate degeneracy of the  $1_1^-$ ,  $2_1^-$ ,  $3_2^-$ ,  $4_1^-$ , and  $5_1^-$  levels, which is considered a quintet of the quadrupole-octupole phonon coupling  $2^+ \otimes 3^-$ . The degeneracy is removed after the mixing, as a consequence of the repulsion among the low-spin levels.

To interpret the nature of the low-lying states, it is useful to analyze fraction of the  $2kp$ - $2kh$  components in their wave functions. The corresponding results for some low-lying states are listed in Table II. Generally, high degree of the mixing appears to be present, particularly in the two lowest  $0^+$  states. The intruder 2p-2h configuration dominates over the normal configuration in the yrast states of both parities for the  $^{72}\text{Ge}$ ,  $^{74}\text{Ge}$ , and  $^{76}\text{Kr}$  nuclei. The 4p-4h configuration associated with the

TABLE II. Fractions (in %) of the  $2kp$ - $2kh$   $[n_k]$  configurations in the *sdf*-IBM wave functions of low-lying states.

$I^\pi$	Config.	$^{72}\text{Ge}$	$^{74}\text{Se}$	$^{74}\text{Kr}$	$^{76}\text{Kr}$
$0_1^+$	$[n_0]$	38	37	25	24
	$[n_1]$	62	63	43	71
	$[n_2]$			32	5
$0_2^+$	$[n_0]$	62	62	19	51
	$[n_1]$	38	38	14	15
	$[n_2]$			67	34
$0_3^+$	$[n_0]$	0.01	3	56	14
	$[n_1]$	99.99	97	42	25
	$[n_2]$			2	61
$2_1^+$	$[n_0]$	8	6	12	4
	$[n_1]$	92	94	24	90
	$[n_2]$			63	6
$2_2^+$	$[n_0]$	4	84	28	0
	$[n_1]$	96	16	36	18
	$[n_2]$			36	82
$4_1^+$	$[n_0]$	2	2	1	2
	$[n_1]$	98	98	5	94
	$[n_2]$			94	4
$3_1^-$	$[n_0]$	28	19	1.8	19
	$[n_1]$	72	81	6.5	75
	$[n_2]$			91.7	6
$4_1^-$	$[n_0]$	4	3	24	3
	$[n_1]$	96	97	39	92
	$[n_2]$			38	5
$5_1^-$	$[n_0]$	5.8	4	0.32	4
	$[n_1]$	94.2	96	2.44	88
	$[n_2]$			97.24	8

strongly deformed prolate minimum makes a particularly large contribution to the low-lying states of  $^{74}\text{Kr}$ .

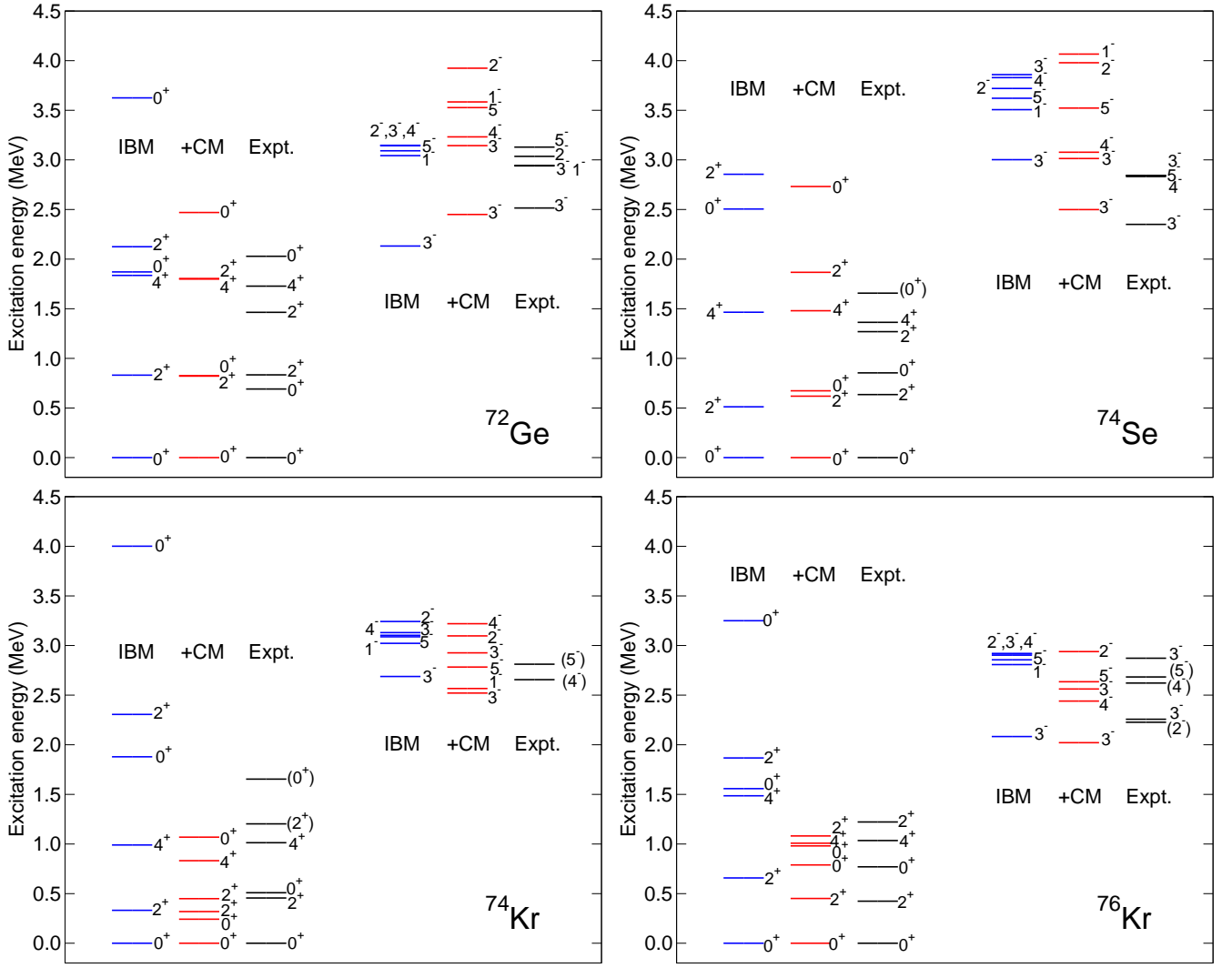


FIG. 3. Comparison of low-energy excitation spectra of positive- and negative-parity states calculated with the *sdf*-IBM excluding (“IBM”) and including (“+CM”) the configuration mixing. Experimental spectra [62] are also shown as a reference.

## B. Detailed energy levels

For each nucleus, low-energy band structure is studied by organizing states according to the structures of the wave functions, some of which are shown in Table II, and to the dominant  $E2$  transitions within bands. The detailed level schemes thus established are shown in Figs. 4–7, for the four studied nuclei.

As shown in Table II, the spherical normal configuration  $[n_0]$  and the oblate 2p-2h configuration  $[n_1]$  are substantially mixed in the ground state  $0_1^+$  of  $^{72}\text{Ge}$ . The ground-state band with spin  $I^\pi \geq 2^+$  is, however, mostly of  $[n_1]$  oblate nature. The calculation gives the  $0_2^+$  band with the bandhead close in energy to the  $2_1^+$  level (see Fig. 4). Furthermore, a quasi- $\gamma$  band, consisting of the  $2_2^+$ ,  $3_1^+$ ,  $4_2^+$ ,  $5_1^+$  states is obtained. The calculated energy level of the  $0_3^+$  state can be compared to the measured

one at the excitation energy  $E_x = 2065$  keV. The  $0_3^+$  state is here suggested to be purely of the 2p-2h oblate nature (99.99%). The  $I^\pi = 3_1^-$  state, calculated at  $E_x = 2450$  keV, is the lowest-energy negative-parity state, and corresponds to the measured one at  $E_x = 2515$  keV [62]. The predicted odd-spin  $\Delta I = 2$  negative-parity band is, however, rather stretched, in comparison with the data, due to the level repulsion. In addition, the  $2_1^-$  state is calculated at  $E_x = 3924$  keV, while the experimental one is at  $E_x = 3036$  keV.

For  $^{74}\text{Se}$ , the calculation gives the low-lying  $0_2^+$  state slightly above the  $2_1^+$  one (Fig. 5). The observed even- and odd-spin  $\Delta I = 2$  positive-parity non-yrast bands with bandhead  $2^+$  and  $3^+$  states are here considerably overestimated. In this calculation, these non-yrast bands are supposed to form a quasi- $\gamma$  band, and are mainly accounted for by the  $[n_1]$  oblate configuration. The discrepancy with the data implies that the triaxiality is not

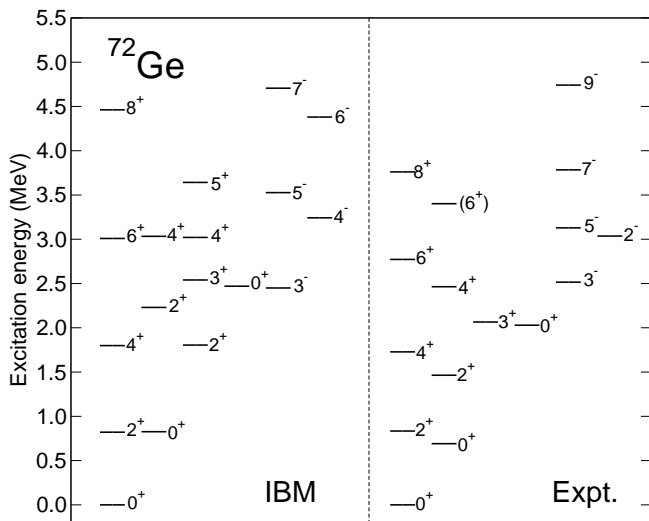


FIG. 4. Low-energy excitation spectra of positive- and negative-parity states of  $^{72}\text{Ge}$  calculated with the configuration mixing *sdf*-IBM in comparison with experimental data [62].

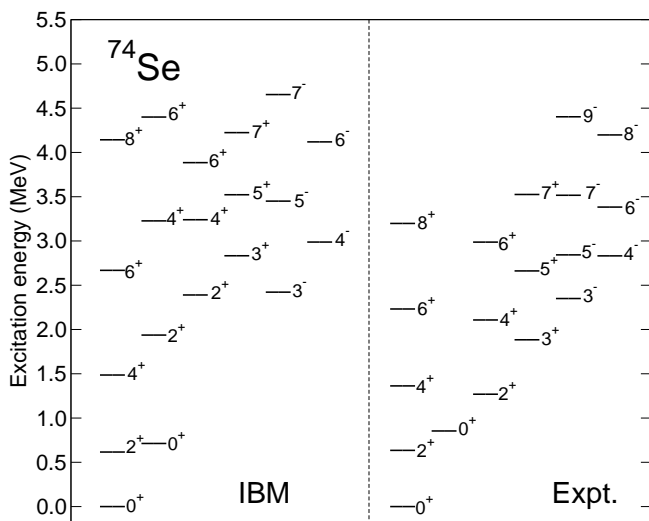


FIG. 5. Same as Fig. 4, but for  $^{74}\text{Se}$ .

sufficiently taken into account in the IBM system. Indeed, as shown in Fig. 1, the mapped triaxial quadrupole energy surface for  $^{74}\text{Se}$  has an oblate ground-state minimum that is rather rigid in the  $\gamma$  deformation, while the corresponding SCMF energy surface is softer. As a consequence, the mapped IBM gives a rotational-like energy spectrum like that shown in Fig. 5, in which the  $\gamma$  bandhead is calculated to be high with respect to the ground-state band.

The low-spin positive-parity states of  $^{74}\text{Kr}$  are here determined by the strong admixture of the three configurations (cf. Table II), with the largest contribution from

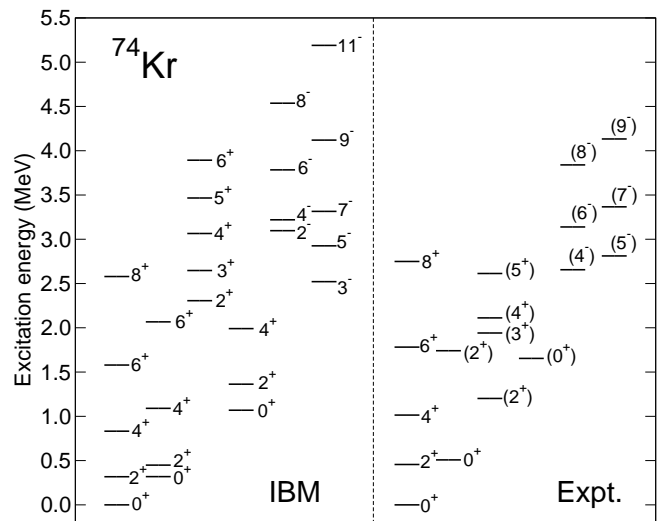


FIG. 6. Same as Fig. 4, but for  $^{74}\text{Kr}$ .

the 2p-2h oblate one. In the ground-state band, the 4p-4h prolate configuration comes to play a dominant role with increasing spin  $I^\pi \geq 2^+$ , and already at  $I^\pi = 4_1^+$  the  $[n_2]$  configuration constitutes 94 % of the wave function. As shown in Fig. 6, the calculation gives the low-energy  $0_2^+$  band, with the bandhead  $0_2^+$  level below the  $2_1^+$  one. The  $0_2^+$  state is here predicted to be mainly made of the strongly deformed prolate configuration. The  $2_2^+$  state is interpreted as the first excited state of the predicted  $0_2^+$  band, and lies close in energy to the bandhead  $0_2^+$ . The data, however, suggest a larger energy gap between the  $0_2^+$  and  $2_3^+$  levels. The proposed quasi- $\gamma$  band, which is built on top of the  $2_4^+$  state, is found at much higher excitation energy than the observed one. One finds a nearly harmonic pattern in the calculated quasi- $\gamma$  band. This contradicts the data, which suggest a pattern typical of a  $\gamma$ -unstable rotor [63], with the  $3^+$  level lying close to the  $4^+$  one. The present calculation further produces another rotational-like band built upon the  $0_3^+$  state at  $E_x = 1069$  keV. The corresponding  $0_3^+$  level has been observed experimentally at  $E_x = 1654$  keV. The  $3_1^-$  state is here calculated to be the lowest negative-parity state, but it is not observed experimentally. The observed even- and odd-spin negative-parity states are the lowest-spin members of the rotational bands [64] that extend up to  $I = 32^-$  and  $I = 35^-$ , respectively.

Figure 7 compares between the calculated and experimental low-energy excitation spectra for  $^{76}\text{Kr}$ . Notable features found in the calculated energy level scheme are the low-energy  $0_2^+$  and  $0_3^+$  excited states, both appearing below the  $4_1^+$  level. The  $0_2^+$  band obtained from the calculation looks like a rotational band, while in the  $0_3^+$  one the energy gap between the  $0_3^+$  bandhead and the first excited state in the band,  $2_4^+$ , is larger than in the  $0_2^+$  band. Experimentally, a  $0_2^+$  band with the bandhead  $0_2^+$  level at  $E_x = 770$  keV is observed. The present calculation



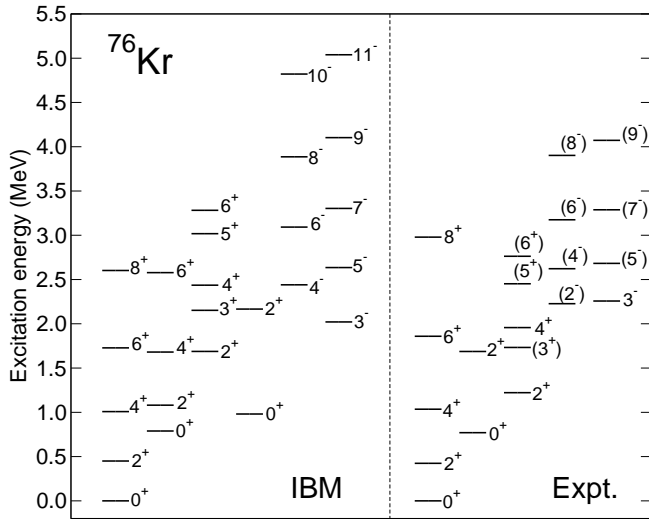


FIG. 7. Same as Fig. 4, but for  $^{76}\text{Kr}$ .

suggests an approximate odd-even-spin staggering in the quasi- $\gamma$  band; that is, the energy levels of the odd- and even-spin members of the band higher than  $I^\pi = 2^+$  are close to each other. This is consistent, both qualitatively and quantitatively, with the observed quasi- $\gamma$  band. Two calculated negative-parity  $\Delta I = 2$  bands, starting from the  $3_1^-$  and  $4_1^-$  levels, can be compared with the observed  $3^-$  and  $2^-$  bands, respectively, which extend up to the spin  $I^\pi = 19^-$  and  $22^-$  states [65]. At variance with the data, the  $2_1^-$  level is calculated to be  $E_x = 2939$  keV, which is above the  $4_1^-$  one. The discrepancy indicates that there may be a missing component within the model, e.g., the dipole,  $p$ , boson degrees of freedom. However, the inclusion of the  $p$  bosons in the considered boson model space is practically so complicated that it is not pursued in this work.

### C. Transition properties

Electric monopole ( $E0$ ), dipole ( $E1$ ), quadrupole ( $E2$ ), and octupole ( $E3$ ) transition properties are calculated with the  $E\lambda$  ( $\lambda = 0, 1, 2$ , and  $3$ ) transition operator that is given by

$$\hat{T}^{E\lambda} = \sum_k \mathcal{P}_k \hat{T}_k^{E\lambda} \mathcal{P}_k. \quad (18)$$

The transition operator  $\hat{T}_k^{E\lambda}$  for each unperturbed space is defined as

$$\begin{aligned} \hat{T}_k^{E0} &= e_{0,k}(\hat{n}_d + \hat{n}_f), & \hat{T}_k^{E1} &= e_{1,k}\hat{D}, \\ \hat{T}_k^{E2} &= e_{2,k}\hat{Q}, & \hat{T}_k^{E3} &= e_{3,k}\hat{O}. \end{aligned}$$

$\hat{D} = (d^\dagger \times \tilde{f} + f^\dagger \times \tilde{d})^{(1)}$  denotes dipole operator, while  $\hat{n}_d$ ,  $\hat{n}_f$ ,  $\hat{Q}$ , and  $\hat{O}$  were already defined. For each  $E\lambda$

transition, the effective charges  $e_{\lambda,k}$  are assumed to be the same for all the configurations included,  $e_{\lambda,0} = e_{\lambda,1} = e_{\lambda,2} \equiv e_\lambda$ .

Table III lists the calculated  $B(E2)$ ,  $B(E3)$ , and  $B(E1)$  transition probabilities,  $\rho^2(E0) = (Z/R_0^2)^2 B(E0)$  values, and the spectroscopic quadrupole moments  $Q^{(s)}$  for low-lying states. Here the  $E0$  and  $E2$  boson charges are adjusted, for each nucleus, to reproduce the experimental  $B(E2; 2_1^+ \rightarrow 0_1^+)$  and  $\rho^2(E0; 0_2^+ \rightarrow 0_1^+)$  values, respectively. For  $^{76}\text{Kr}$ , since the corresponding  $E0$  datum is not available, the same  $e_0$  value as the one for  $^{74}\text{Kr}$  is used. The adopted  $e_2$  ( $e_0$ ) values for  $^{72}\text{Ge}$ ,  $^{74}\text{Se}$ ,  $^{74}\text{Kr}$ , and  $^{76}\text{Kr}$  are, respectively, 0.052 (0.078), 0.061 (0.12), 0.056 (0.18), and 0.077 (0.18) eb (fm). The  $E1$  and  $E3$  boson charges,  $e_1 = 0.036$  eb $^{1/2}$  and  $e_3 = 0.042$  eb $^{3/2}$ , are fitted to reproduce the experimental  $B(E1; 3_1^- \rightarrow 2_1^+)$  and  $B(E3; 3_1^- \rightarrow 0_1^+)$  values for  $^{72}\text{Ge}$  and  $^{74}\text{Se}$ , respectively, and are kept constant for all four nuclei.

The present calculation yields the interband transition rates, including  $B(E2; 0_2^+ \rightarrow 2_1^+)$  and  $B(E2; 2_2^+ \rightarrow 2_1^+)$  ones, larger than or of the same order of magnitude as that for the  $B(E2; 2_1^+ \rightarrow 0_1^+)$  one. The large interband  $E2$  transitions are a consequence of the configuration mixing. The  $B(E3; 3_1^- \rightarrow 0_1^+)$  rate is often considered a signature of the octupolarity, and is here calculated to be in the range 20-30 W.u., with the fixed  $e_3$  boson charge. The  $3_1^- \rightarrow 0_2^+$   $E3$  transition is orders of magnitude weaker than the  $3_1^- \rightarrow 0_1^+$  one for  $^{72}\text{Ge}$ ,  $^{74}\text{Se}$ , and  $^{76}\text{Kr}$ , while it is of the same order of magnitude as the  $3_1^- \rightarrow 0_1^+$  transition in  $^{74}\text{Kr}$ . This further confirms the strong configuration mixing in the  $0_2^+$  state for  $^{74}\text{Kr}$ . The model further provides the  $E1$  properties, and particularly large  $B(E1; 3_1^- \rightarrow 2_1^+)$  and  $B(E1; 5_1^- \rightarrow 4_1^+)$  values are obtained for  $^{74}\text{Kr}$ . The  $E0$  transition serves as an empirical signature of shape coexistence, and the nuclei in this mass region are expected to show pronounced  $E0$  transitions, especially, between the low-lying  $0^+$  states. For  $^{74}\text{Kr}$  and  $^{76}\text{Kr}$ , the  $E0$  transitions between the  $0_3^+$  and  $0_2^+$  states are also as strong as that between the  $0_1^+$  and  $0_2^+$  ones.

The positive  $Q^{(s)}(2_1^+)$  values obtained for  $^{72}\text{Ge}$  and  $^{74}\text{Se}$  imply an oblate deformation, but are at variance with the experimental values [24], which are negative and hence suggest prolate nature for both nuclei. The wrong sign of the calculated  $Q^{(s)}(2_1^+)$  is due to the fact that the  $2_1^+$  states of both  $^{72}\text{Ge}$  and  $^{74}\text{Se}$  are predominantly determined by the 2p-2h oblate configuration (see Table II), since the SCMF calculations with the chosen EDF give a pronounced oblate minimum. The positive  $Q^{(s)}(2_2^+)$  value for  $^{72}\text{Ge}$  also indicates the oblate nature of the  $2_2^+$  state. For  $^{74}\text{Se}$ , on the other hand, the  $2_2^+$  state is dominated by the 0p-0h nearly spherical configuration, and the quadrupole moment is calculated to be rather small in magnitude,  $Q^{(s)}(2_2^+) < 0.1$ . Similar conclusions on the  $Q^{(s)}$  moments have been drawn, both quantitatively and qualitatively, from the previous configuration-mixing  $sd$ -IBM studies on the Ge and Se isotopes, using the Gogny-type EDF [68]. The Gogny-EDF calculation carried out

TABLE III. Calculated and experimental  $B(E2)$ ,  $B(E3)$ , and  $B(E1)$  transition probabilities (in W.u.),  $\rho^2(E0)$  values, and spectroscopic quadrupole moments  $Q^{(s)}$  (in eb). The experimental data are adopted from Refs. [24, 62, 66, 67].

	$^{72}\text{Ge}$		$^{74}\text{Se}$		$^{74}\text{Kr}$		$^{76}\text{Kr}$	
	Calc.	Expt.	Calc.	Expt.	Calc.	Expt.	Calc.	Expt.
$B(E2; 2_1^+ \rightarrow 0_1^+)$	23.5	$23.5 \pm 0.4$	42.0	$42.0 \pm 0.6$	66	$66 \pm 1$	75	$75 \pm 1$
$B(E2; 4_1^+ \rightarrow 2_1^+)$	42	$37 \pm 5$	79	$80 \pm 4$	107	$154 \pm 5$	135	$129 \pm 3$
$B(E2; 6_1^+ \rightarrow 4_1^+)$	48	$37^{+21}_{-37}$	90	$72 \pm 15$	147	$163 \pm 16$	155	$146^{+16}_{-5}$
$B(E2; 0_2^+ \rightarrow 2_1^+)$	29	$89 \pm 2$	63	$77 \pm 7$	83	$255 \pm 25$	73	$126^{+6}_{-5}$
$B(E2; 2_2^+ \rightarrow 2_1^+)$	33	$62^{+9}_{-11}$	6.8	$48 \pm 14$	94	$25 \pm 4$	35	1
$B(E2; 2_2^+ \rightarrow 0_1^+)$	0.57	$0.130^{+0.018}_{-0.024}$	4.1	$0.80 \pm 0.23$	2.0	$4.3 \pm 0.5$	1.9	4
$B(E2; 2_2^+ \rightarrow 0_2^+)$	0.060	$0.030^{+0.005}_{-0.006}$	22		65	$24 \pm 4$	32	157
$B(E3; 3_1^- \rightarrow 0_1^+)$	29	$29 \pm 6$	23	$9 \pm 2$	30		33	
$B(E3; 3_1^- \rightarrow 0_2^+)$	0.27		0.44		25		0.0013	
$B(E3; 3_1^- \rightarrow 2_1^+)$	15		14		49		12	
$B(E3; 3_1^- \rightarrow 2_2^+)$	0.0084		0.45		13		4.5	
$B(E3; 5_1^- \rightarrow 2_1^+)$	21		15		29		15	
$B(E1; 3_1^- \rightarrow 2_1^+) \times 10^5$	12		0.115	$0.115 \pm 0.021$	36		8.5	
$B(E1; 3_1^- \rightarrow 2_2^+) \times 10^5$	26		13		5.8		5.7	
$B(E1; 3_1^- \rightarrow 4_1^+) \times 10^5$	2.0	$4.8 \pm 1.0$	5.6	$0.38 \pm 0.10$	9.3		1.5	
$B(E1; 5_1^- \rightarrow 4_1^+) \times 10^5$	134		96		341		104	
$\rho^2(E0; 0_2^+ \rightarrow 0_1^+) \times 10^3$	9.17	$9.18 \pm 0.02$	23.2	$23.1 \pm 2.2$	113	$113 \pm 27$	51	
$\rho^2(E0; 0_3^+ \rightarrow 0_1^+) \times 10^3$	0.00031		0.35		28		0.19	
$\rho^2(E0; 0_3^+ \rightarrow 0_2^+) \times 10^3$	0.00026		0.41		43		122	
$\rho^2(E0; 2_2^+ \rightarrow 2_1^+) \times 10^3$	0.047		4.9		107		6.0	
$Q^{(s)}(2_1^+)$	0.22	$-0.13 \pm 0.06$	0.59	$-0.36 \pm 0.07$	-0.33	$-0.53^{+0.24}_{-0.23}$	0.70	$-0.7 \pm 0.2$
$Q^{(s)}(2_2^+)$	-0.18		0.046		0.094	$0.24^{+0.21}_{-0.17}$	-0.92	$-0.7 \pm 0.3$
$Q^{(s)}(2_3^+)$	0.044		-0.46		0.60	$0.3^{+0.9}_{-0.3}$	-0.45	$1.0 \pm 0.4$

in that reference also predicted the oblate global minimum in the triaxial quadrupole energy surfaces for both  $^{72}\text{Ge}$  and  $^{74}\text{Se}$ .

The predicted  $Q^{(s)}(2_1^+)$  and  $Q^{(s)}(2_2^+)$  for  $^{74}\text{Kr}$  are within uncertainties of the observed values [24] and the sign is consistent with the data. The negative  $Q^{(s)}(2_1^+)$  value reflects the fact that the  $2_1^+$  state is composed mainly of the 4p-4h prolate configuration (cf. Table II). In the  $2_2^+$  wave function of the same nucleus, the oblate 0p-0h and 2p-2h configurations are more dominant, hence the corresponding quadrupole moment has positive sign. For  $^{76}\text{Kr}$ , the model yields  $Q^{(s)}(2_1^+) > 0$ , which indicates oblate ground state but contradicts the data. Note that the  $2_1^+$  state for  $^{76}\text{Kr}$  is mainly accounted for by the 2p-2h oblate configuration, while the prolate 4p-4h configuration plays only a minor role. The negative quadrupole moment  $Q^{(s)}(2_2^+) = -0.92$  eb, obtained by the present calculation, is consistent with the experimental value.

The configuration mixing has an influence on qualitative features of some transition properties of the low-lying states, especially those that involve the excited  $0^+$  states. Table IV lists the ratios of  $B(E2)$ ,  $B(E1)$ , and  $B(E3)$  transition probabilities, and the  $E0/E2$  ratio defined as  $X(E0/E2) \equiv \rho^2(E0; 0_2^+ \rightarrow 0_1^+)e^2R_0^4/B(E2; 0_2^+ \rightarrow 2_1^+)$ , that are obtained from the *sdf*-IBM calculations with and without the configuration mixing. The configura-

tion mixing does not have much influence on the  $B(E2; 4_1^+ \rightarrow 2_1^+)/B(E2; 2_1^+ \rightarrow 0_1^+)$  ratio of the inband transitions, but increases the  $B(E2; 0_2^+ \rightarrow 2_1^+)/B(E2; 2_1^+ \rightarrow 0_1^+)$  one for  $^{74}\text{Se}$  and  $^{74}\text{Kr}$  by a factor of 5. Both the  $B(E1; 3_1^- \rightarrow 4_1^+)/B(E1; 3_1^- \rightarrow 2_1^+)$  and  $B(E3; 3_1^- \rightarrow 2_1^+)/B(E3; 3_1^- \rightarrow 0_1^+)$  ratios are generally increased by orders of magnitude. The  $X(E0/E2)$  ratio is significantly reduced for most of the nuclei, and becomes more consistent with the data [66] after the mixing.

#### D. Sensitivity to the truncation of the $f$ boson number

The results presented so far have been obtained with the maximum number of  $f$  bosons,  $n_f^{\max}$ , being truncated as  $n_f^{\max} = 3$  for each  $[n_k]$  subspace. To confirm that this truncation is adequate, calculated  $\rho^2(E0)$  values,  $B(E2)$ ,  $B(E3)$ , and  $B(E1)$  transition rates, and spectroscopic quadrupole moments  $Q^{(s)}$  are shown in Fig. 8 as functions of  $n_f^{\max}$ . One realizes that the calculated quantities generally become stable for  $n_f^{\max} \geq 2$ . This, in turn, indicates that more than one  $f$  boson should be needed in the considered boson model space to obtain converged

TABLE IV.  $B(E2)$ ,  $B(E1)$ ,  $B(E3)$ , and  $X(E0/E2)$  ratios, calculated by the *sdf*-IBM with (“IBM”) and without (“+CM”) the configuration mixing. The experimental data are obtained from Refs. [62, 66, 67].

	$^{72}\text{Ge}$			$^{74}\text{Se}$			$^{74}\text{Kr}$			$^{76}\text{Kr}$		
	IBM	+CM	Expt.	IBM	+CM	Expt.	IBM	+CM	Expt.	IBM	+CM	Expt.
$B(E2; 4_1^+ \rightarrow 2_1^+)$	1.60	1.77	$1.57 \pm 0.21$	1.45	1.88	$1.90 \pm 0.10$	1.46	1.62	$2.33 \pm 0.08$	1.70	1.80	$1.72 \pm 0.05$
$B(E2; 2_1^+ \rightarrow 0_1^+)$												
$B(E2; 0_2^+ \rightarrow 2_1^+)$	1.00	1.22	$3.79 \pm 0.11$	0.27	1.50	$1.83 \pm 0.17$	0.24	1.25	$3.86 \pm 0.38$	1.20	0.98	$1.68_{-0.07}^{+0.08}$
$B(E2; 2_1^+ \rightarrow 0_1^+)$												
$B(E2; 2_2^+ \rightarrow 0_2^+)$	0.14	0.003	$0.0013 \pm 0.0002$	0.30	0.52		0.34	0.98	$0.36 \pm 0.06$	0.28	0.43	$2.09 \pm 0.03$
$B(E2; 2_1^+ \rightarrow 0_1^+)$												
$B(E2; 2_2^+ \rightarrow 0_2^+)$	2.7	0.11	$0.23_{-0.06}^{+0.05}$	16	5.4		36	33	$5.58 \pm 1.13$	8.3	17	39
$B(E2; 2_2^+ \rightarrow 0_1^+)$												
$B(E1; 3_1^- \rightarrow 4_1^+)$	0.018	0.17		0.51	49		3.3	0.26		0.064	0.18	
$B(E1; 3_1^- \rightarrow 2_1^+)$												
$B(E3; 3_1^- \rightarrow 2_1^+)$	0.057	0.50		0.015	0.59		0.61	1.65		0.036	0.35	
$B(E3; 3_1^- \rightarrow 0_1^+)$												
$10^3 \rho^2(E0; 0_2^+ \rightarrow 0_1^+) e^2 R_0^4$	37	11		444	13	$17 \pm 4$	130	48	$10.5 \pm 4.8$	211	24	
$B(E2; 0_2^+ \rightarrow 2_1^+)$												

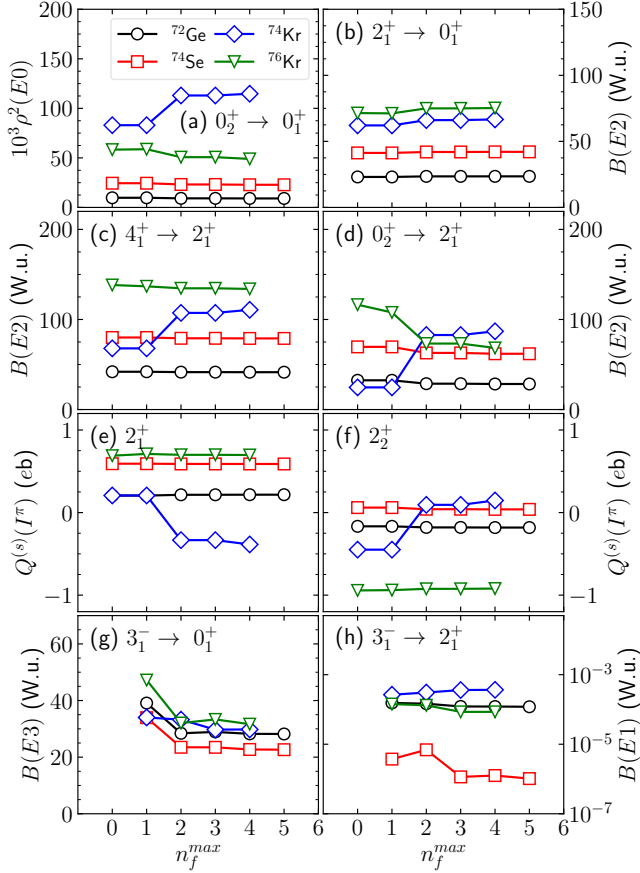


FIG. 8. Calculated transition properties of  $^{72}\text{Ge}$ ,  $^{74}\text{Se}$ ,  $^{74}\text{Kr}$ , and  $^{76}\text{Kr}$  as functions of the maximum number of  $f$  bosons,  $n_f^{\max}$ : (a)  $\rho^2(E0; 0_2^+ \rightarrow 0_1^+)$ , (b)  $B(E2; 2_1^+ \rightarrow 0_1^+)$ , (c)  $B(E2; 4_1^+ \rightarrow 2_1^+)$ , (d)  $B(E2; 0_2^+ \rightarrow 2_1^+)$ , (e)  $Q^{(s)}(I^\pi; 2_1^+)$ , (f)  $Q^{(s)}(I^\pi; 2_2^+)$ , (g)  $B(E3; 3_1^- \rightarrow 0_1^+)$ , and (h)  $B(E1; 3_1^- \rightarrow 2_1^+)$ . The same boson effective charges are used for each set of the calculations corresponding to different  $n_f^{\max}$ .

results.

It is, nevertheless, worth noting that many of the transition properties calculated for  $^{74}\text{Kr}$  change significantly from  $n_f^{\max} = 1$  to 2, an illustrative example being the  $Q^{(s)}(2_1^+)$  and  $Q^{(s)}(2_2^+)$  moments for which the sign changes at  $n_f^{\max} = 2$ . Since for  $^{74}\text{Kr}$  the 4p-4h prolate components make large contributions to the low-lying states, the structure of the  $2_1^+$  wave function is supposed to be sensitive to the increasing  $n_f^{\max}$ : For  $n_f^{\max} = 1$  ( $n_f^{\max} = 2$ ), the three configurations  $[n_0]$ ,  $[n_1]$ , and  $[n_2]$  constitute 12 (28) %, 24 (45) %, and 63 (27) % of the  $2_1^+$  wave function of  $^{74}\text{Kr}$ . A similar argument holds for the  $2_2^+$  state.

On the other hand, the truncation for  $n_f^{\max}$  does not have as noticeable impacts on the excitation energies as in the case of the transition properties, and hence these are not discussed here.

## V. CONCLUDING REMARKS

Based on the nuclear density functional theory, configuration mixing and octupole degrees of freedom are incorporated microscopically in the interacting boson model. The constrained SCMF calculations using the universal EDF and pairing interaction provide two sets of the potential energy surfaces, one with the triaxial quadrupole, and the other with the axially symmetric quadrupole and octupole degrees of freedom. A model Hamiltonian for the configuration mixing *sdf*-IBM is determined by mapping the SCMF energy surfaces onto the bosonic counterparts.

In the illustrative application to the transitional nuclei  $^{72}\text{Ge}$ ,  $^{74}\text{Se}$ ,  $^{74}\text{Kr}$ , and  $^{76}\text{Kr}$ , the configuration mixing of the normal and intruder states in the *sdf*-IBM significantly lowers the  $0_2^+$  energy level. The predicted low-energy positive-parity states are characterized by the

strong admixture of the nearly spherical, weakly deformed oblate, and strongly deformed prolate shapes. In particular, the prolate deformation plays an important role in the ground state of  $^{74}\text{Kr}$ . The configuration mixing has influences on the transition properties, as well as the excitation energies. Notable examples are the increase of the  $B(E2; 0_2^+ \rightarrow 2_1^+)$  transition rate and the reduction of the  $X(E0/E2)$  ratio after the mixing, both of which quantities are signatures of shape coexistence and mixing. For the  $N = 40$  isotones, on the other hand, the model calculation predicts the spectroscopic quadrupole moments of the  $2_1^+$  state with positive sign, which contradicts experiment. The discrepancy arises from the fact that large amounts of the oblate components are contained in the corresponding  $2_1^+$  wave functions. The nature of the IBM wave functions reflects the topology of the SCMF potential energy surfaces, which indeed suggest the pronounced oblate minimum in these nuclei. The mapped Hamiltonian produces negative-parity bands with the lowest-energy state with  $I^\pi = 3_1^-$  at the excitation energy  $E_x \approx 2$  MeV, and the electric octupole transitions to the ground state. The low-energy negative-parity states are here shown to be made predominantly

of the deformed intruder configurations.

The proposed model can be used further for extensive studies on neutron-rich nuclei, in which both shape coexistence and octupole collectivity are expected to play an important role at low energy, and which are experimentally of much interest.

## ACKNOWLEDGMENTS

This work is financed within the Tenure Track Pilot Programme of the Croatian Science Foundation and the École Polytechnique Fédérale de Lausanne, and the Project TTP-2018-07-3554 Exotic Nuclear Structure and Dynamics, with funds of the Croatian-Swiss Research Programme.

### Appendix A: Formulas for the bosonic potential energy surface

In the diagonal element of the matrix  $\mathbf{E}(\beta_2, \gamma, \beta_3)$ , Eq. (13), the expectation value of the unperturbed Hamiltonian reads

$$\begin{aligned} \langle \Psi_k(\vec{\alpha}_k) | \hat{H}_k | \Psi_k(\vec{\alpha}_k) \rangle &= \frac{n_k(\tilde{\epsilon}_{s,k} + \tilde{\epsilon}_{d,k}\beta_{2,k}^2 + \tilde{\epsilon}_{f,k}\beta_{3,k}^2)}{1 + \beta_{2,k}^2 + \beta_{3,k}^2} + \frac{n_k(n_k - 1)}{(1 + \beta_{2,k}^2 + \beta_{3,k}^2)^2} \\ &\times \left[ \kappa_{2,k} \left[ 4\beta_{2,k}^2 - 4\tilde{\chi}_k\beta_{2,k}^3 \cos 3\gamma + \tilde{\chi}_k^2\beta_{2,k}^4 + \tilde{\chi}'_k\beta_{2,k}\beta_{3,k}^2 \{4 - \tilde{\chi}_k\beta_{2,k}(3 \cos 2\gamma - 1)\} + \tilde{\chi}''_k\beta_{3,k}^4 \right] \right. \\ &\left. - 4\kappa_{3,k}\beta_{3,k}^2 \left\{ 1 + 2\tilde{\chi}''_k\beta_{2,k} + \frac{1}{8}\beta_{2,k}^2\tilde{\chi}''_k{}^2(9 - \cos 2\gamma) \right\} \right] + \frac{1}{30}\eta_k \frac{n_k(n_k - 1)(n_k - 2)}{(1 + \beta_{2,k}^2 + \beta_{3,k}^2)^3} \beta_{2,k}^6 \sin^2 3\gamma. \quad (\text{A1}) \end{aligned}$$

Note that, in the first line of the above expression,  $\tilde{\epsilon}_{s,k} = 5\kappa_{2,k} - 7\kappa_{3,k}$ ,  $\tilde{\epsilon}_{d,k} = \epsilon_{d,k} + (1 + \chi_k^2)\kappa_{2,k} - 6\rho_k - \frac{7}{5}\chi_k''^2\kappa_{3,k}$ , and  $\tilde{\epsilon}_{f,k} = \epsilon_{f,k} - \frac{5}{7}\chi_k'^2\kappa_{2,k} + (1 + \chi_k''^2)\kappa_{3,k}$ , and that

$\tilde{\chi}_k \equiv \sqrt{\frac{2}{7}}\chi_k$ ,  $\tilde{\chi}'_k \equiv \frac{2}{\sqrt{21}}\chi'_k$ , and  $\tilde{\chi}''_k \equiv -\frac{2}{\sqrt{15}}\chi''_k$ . Nondiagonal elements of  $\mathbf{E}(\beta_2, \gamma, \beta_3)$ , Eq. (14), coming from the mixing interaction  $\hat{V}_{k,k+1}$ , with  $k = 0$  or  $1$ , are calculated as

$$\begin{aligned} E_{k,k+1}(\beta_2, \gamma, \beta_3) &= E_{k+1,k}(\beta_2, \gamma, \beta_3) \\ &= \sqrt{(n_k + 1)n_{k+1}} \frac{\omega_{s,k} + \omega_{d,k}\beta_{2,k+1}^2 + \omega_{f,k}\beta_{3,k+1}^2}{1 + \beta_{2,k+1}^2 + \beta_{3,k+1}^2} \left[ \frac{1 + \beta_{2,k}\beta_{2,k+1} + \beta_{3,k}\beta_{3,k+1}}{\sqrt{(1 + \beta_{2,k}^2 + \beta_{3,k}^2)(1 + \beta_{2,k+1}^2 + \beta_{3,k+1}^2)}} \right]^{n_k}. \quad (\text{A2}) \end{aligned}$$

[1] K. Heyde, P. Van Isacker, M. Waroquier, J. L. Wood, and R. A. Meyer, *Phys. Rep.* **102**, 291 (1983).

[2] J. L. Wood, K. Heyde, W. Nazarewicz, M. Huyse, and

- P. van Duppen, *Phys. Rep.* **215**, 101 (1992).
- [3] A. N. Andreyev, M. Huyse, P. Van Duppen, L. Weissman, D. Ackermann, J. Gerl, F. P. Hessberger, S. Hofmann, A. Kleinböhl, G. Münzenberg, S. Reshitko, C. Schlegel, H. Schaffner, P. Cagarda, M. Matos, S. Saro, A. Keenan, C. Moore, C. D. O'Leary, R. D. Page, M. Taylor, H. Kettunen, M. Leino, A. Lavrentiev, R. Wyss, and K. Heyde, *Nature (London)* **405**, 430 (2000).
- [4] K. Heyde and J. L. Wood, *Rev. Mod. Phys.* **83**, 1467 (2011).
- [5] P. Federman and S. Pittel, *Phys. Lett. B* **69**, 385 (1977).
- [6] P. Van Duppen, E. Coenen, K. Deneffe, M. Huyse, K. Heyde, and P. Van Isacker, *Phys. Rev. Lett.* **52**, 1974 (1984).
- [7] K. Heyde, P. Van Isacker, R. F. Casten, and J. L. Wood, *Phys. Lett. B* **155**, 303 (1985).
- [8] K. Heyde and R. A. Meyer, *Phys. Rev. C* **37**, 2170 (1988).
- [9] K. Heyde, C. De Coster, J. Jolie, and J. L. Wood, *Phys. Rev. C* **46**, 541 (1992).
- [10] K. Heyde, J. Jolie, H. Lehmann, C. De Coster, and J. Wood, *Nucl. Phys. A* **586**, 1 (1995).
- [11] R. Bengtsson, T. Bengtsson, J. Dudek, G. Leander, W. Nazarewicz, and J. ye Zhang, *Phys. Lett. B* **183**, 1 (1987).
- [12] R. Bengtsson and W. Nazarewicz, *Z. Phys. A* **334**, 269 (1989).
- [13] W. Nazarewicz, *Phys. Lett. B* **305**, 195 (1993).
- [14] T. Duguet, M. Bender, P. Bonche, and P.-H. Heenen, *Phys. Lett. B* **559**, 201 (2003).
- [15] R. R. Rodríguez-Guzmán, J. L. Egido, and L. M. Robledo, *Phys. Rev. C* **69**, 054319 (2004).
- [16] Z. P. Li, T. Nikšić, and D. Vretenar, *J. Phys. G: Nucl. Part. Phys.* **43**, 024005 (2016).
- [17] P. A. Butler and W. Nazarewicz, *Rev. Mod. Phys.* **68**, 349 (1996).
- [18] P. A. Butler, *J. Phys. G: Nucl. Part. Phys.* **43**, 073002 (2016).
- [19] L. P. Gaffney, P. A. Butler, M. Scheck, A. B. Hayes, F. Wenander, M. Albers, B. Bastin, C. Bauer, A. Blazhev, S. Bönig, N. Bree, J. Cederkäll, T. Chupp, D. Cline, T. E. Cocolios, T. Davinson, H. D. Witte, J. Diriken, T. Grahm, A. Herzan, M. Huyse, D. G. Jenkins, D. T. Joss, N. Kesteloot, J. Konki, M. Kowalczyk, T. Kröll, E. Kwan, R. Lutter, K. Moschner, P. Napiorkowski, J. Pakarinen, M. Pfeiffer, D. Radeck, P. Reiter, K. Reynders, S. V. Rigby, L. M. Robledo, M. Rudigier, S. Sambhi, M. Seidlitz, B. Siebeck, T. Stora, P. Thoele, P. V. Duppen, M. J. Vermeulen, M. von Schmid, D. Voulot, N. Warr, K. Wimmer, K. Wrzosek-Lipska, C. Y. Wu, and M. Zielinska, *Nature (London)* **497**, 199 (2013).
- [20] M. M. R. Chishti, D. O'Donnell, G. Battaglia, M. Bowry, D. A. Jaroszynski, B. S. N. Singh, M. Scheck, P. Spagnoletti, and J. F. Smith, *Nat. Phys.* **16**, 853 (2020).
- [21] B. Bucher, S. Zhu, C. Y. Wu, R. V. F. Janssens, D. Cline, A. B. Hayes, M. Albers, A. D. Ayangeakaa, P. A. Butler, C. M. Campbell, M. P. Carpenter, C. J. Chiara, J. A. Clark, H. L. Crawford, M. Cromaz, H. M. David, C. Dickerson, E. T. Gregor, J. Harker, C. R. Hoffman, B. P. Kay, F. G. Kondev, A. Korichi, T. Lauritsen, A. O. Macchiavelli, R. C. Pardo, A. Richard, M. A. Riley, G. Savard, M. Scheck, D. Seweryniak, M. K. Smith, R. Vondrasek, and A. Wiens, *Phys. Rev. Lett.* **116**, 112503 (2016).
- [22] B. Bucher, S. Zhu, C. Y. Wu, R. V. F. Janssens, R. N. Bernard, L. M. Robledo, T. R. Rodríguez, D. Cline, A. B. Hayes, A. D. Ayangeakaa, M. Q. Buckner, C. M. Campbell, M. P. Carpenter, J. A. Clark, H. L. Crawford, H. M. David, C. Dickerson, J. Harker, C. R. Hoffman, B. P. Kay, F. G. Kondev, T. Lauritsen, A. O. Macchiavelli, R. C. Pardo, G. Savard, D. Seweryniak, and R. Vondrasek, *Phys. Rev. Lett.* **118**, 152504 (2017).
- [23] P. A. Butler, *Proc. R. Soc. A* **476**, 20200202 (2020).
- [24] E. Clément, A. Gørgen, W. Korten, E. Bouchez, A. Chatillon, J.-P. Delaroche, M. Girod, H. Goutte, A. Hüerstel, Y. L. Coz, A. Obertelli, S. Péru, C. Theisen, J. N. Wilson, M. Zielinska, C. Andreoiu, F. Becker, P. A. Butler, J. M. Casandjian, W. N. Catford, T. Czosnyka, G. d. France, J. Gerl, R.-D. Herzberg, J. Iwanicki, D. G. Jenkins, G. D. Jones, P. J. Napiorkowski, G. Sletten, and C. N. Timis, *Phys. Rev. C* **75**, 054313 (2007).
- [25] E. Clément, M. Zielinska, A. Gørgen, W. Korten, S. Péru, J. Libert, H. Goutte, S. Hilaire, B. Bastin, C. Bauer, A. Blazhev, N. Bree, B. Bruyneel, P. A. Butler, J. Butterworth, P. Delahaye, A. Dijon, D. T. Doherty, A. Ekström, C. Fitzpatrick, C. Fransen, G. Georgiev, R. Gernhäuser, H. Hess, J. Iwanicki, D. G. Jenkins, A. C. Larsen, J. Ljungvall, R. Lutter, P. Marley, K. Moschner, P. J. Napiorkowski, J. Pakarinen, A. Petts, P. Reiter, T. Renström, M. Seidlitz, B. Siebeck, S. Siem, C. Sotty, J. Srebrny, I. Stefanescu, G. M. Tveten, J. Van de Walle, M. Vermeulen, D. Voulot, N. Warr, F. Wenander, A. Wiens, H. De Witte, and K. Wrzosek-Lipska, *Phys. Rev. Lett.* **116**, 022701 (2016).
- [26] C. Kremer, S. Aslanidou, S. Bassauer, M. Hilcker, A. Krugmann, P. von Neumann-Cosel, T. Otsuka, N. Pietralla, V. Y. Ponomarev, N. Shimizu, M. Singer, G. Steinhilber, T. Togashi, Y. Tsunoda, V. Werner, and M. Zweidinger, *Phys. Rev. Lett.* **117**, 172503 (2016).
- [27] R.-B. Gerst, A. Blazhev, K. Moschner, P. Doornenbal, A. Obertelli, K. Nomura, J.-P. Ebran, S. Hilaire, J. Libert, G. Authelet, H. Baba, D. Calvet, F. Château, S. Chen, A. Corsi, A. Delbart, J.-M. Gheller, A. Giganon, A. Gillibert, V. Lapoux, T. Motobayashi, M. Niikura, N. Paul, J.-Y. Roussé, H. Sakurai, C. Santamaria, D. Steppenbeck, R. Taniuchi, T. Uesaka, T. Ando, T. Arici, F. Browne, A. M. Bruce, R. Carroll, L. X. Chung, M. L. Cortés, M. Dewald, B. Ding, F. Flavigny, S. Franchoo, M. Górska, A. Gottardo, J. Jolie, A. Jungclauss, J. Lee, M. Lettmann, B. D. Linh, J. Liu, Z. Liu, C. Lizarazo, S. Momiyama, S. Nagamine, N. Nakatsuka, C. R. Nita, C. Nobs, L. Olivier, R. Orlandi, Z. Patel, Z. Podolyák, M. Rudigier, T. Saito, C. Shand, P.-A. Söderström, I. Stefan, V. Vaquero, V. Werner, K. Wimmer, and Z. Xu, *Phys. Rev. C* **105**, 024302 (2022).
- [28] A. Mukherjee, S. Bhattacharya, T. Trivedi, R. P. Singh, S. Muralithar, D. Negi, R. Palit, S. Nag, S. Rajbanshi, M. K. Raju, S. Kumar, D. Choudhury, R. Kumar, R. K. Bhowmik, S. C. Pancholi, and A. K. Jain, *Phys. Rev. C* **105**, 014322 (2022).
- [29] M. Bender, P.-H. Heenen, and P.-G. Reinhard, *Rev. Mod. Phys.* **75**, 121 (2003).
- [30] T. Nikšić, D. Vretenar, and P. Ring, *Prog. Part. Nucl. Phys.* **66**, 519 (2011).
- [31] L. M. Robledo, T. R. Rodríguez, and R. R. Rodríguez-Guzmán, *J. Phys. G: Nucl. Part. Phys.* **46**, 013001 (2019).
- [32] P. E. Garrett, H. Lehmann, J. Jolie, C. A. McGrath, M. Yeh, and S. W. Yates, *Phys. Rev. C* **59**, 2455 (1999).

- [33] H. Lehmann, A. Nord, A. E. de Almeida Pinto, O. Beck, J. Besserer, P. von Brentano, S. Drissi, T. Eckert, R.-D. Herzberg, D. Jäger, J. Jolie, U. Kneissl, J. Margraf, H. Maser, N. Pietralla, and H. H. Pitz, *Phys. Rev. C* **60**, 024308 (1999).
- [34] D. Bandyopadhyay, C. C. Reynolds, S. R. Leshner, C. Fransen, N. Boukharouba, M. T. McEllistrem, and S. W. Yates, *Phys. Rev. C* **68**, 014324 (2003).
- [35] T. Otsuka, A. Arima, F. Iachello, and I. Talmi, *Phys. Lett. B* **76**, 139 (1978).
- [36] T. Otsuka, A. Arima, and F. Iachello, *Nucl. Phys. A* **309**, 1 (1978).
- [37] P. D. Duval and B. R. Barrett, *Phys. Lett. B* **100**, 223 (1981).
- [38] P. D. Duval and B. R. Barrett, *Nucl. Phys. A* **376**, 213 (1982).
- [39] P. Van Isacker and J.-Q. Chen, *Phys. Rev. C* **24**, 684 (1981).
- [40] K. Heyde, P. Van Isacker, M. Waroquier, and J. Moreau, *Phys. Rev. C* **29**, 1420 (1984).
- [41] R. Casten, P. von Brentano, K. Heyde, P. Van Isacker, and J. Jolie, *Nucl. Phys. A* **439**, 289 (1985).
- [42] K. Nomura, N. Shimizu, D. Vretenar, T. Nikšić, and T. Otsuka, *Phys. Rev. Lett.* **108**, 132501 (2012).
- [43] A. E. L. Dieperink, O. Scholten, and F. Iachello, *Phys. Rev. Lett.* **44**, 1747 (1980).
- [44] J. N. Ginocchio and M. W. Kirson, *Nucl. Phys. A* **350**, 31 (1980).
- [45] A. Bohr and B. R. Mottelson, *Phys. Scr.* **22**, 468 (1980).
- [46] A. Frank, P. Van Isacker, and C. E. Vargas, *Phys. Rev. C* **69**, 034323 (2004).
- [47] A. Bohr and B. R. Mottelson, *Nuclear Structure*, Vol. II (Benjamin, New York, USA, 1975).
- [48] A. Frank, P. Van Isacker, and F. Iachello, *Phys. Rev. C* **73**, 061302 (2006).
- [49] P. Ring and P. Schuck, *The Nuclear Many-Body Problem* (Springer-Verlag, Berlin, 1980).
- [50] D. Vretenar, A. V. Afanasjev, G. A. Lalazissis, and P. Ring, *Phys. Rep.* **409**, 101 (2005).
- [51] T. Nikšić, N. Paar, D. Vretenar, and P. Ring, *Comput. Phys. Commun.* **185**, 1808 (2014).
- [52] T. Nikšić, D. Vretenar, and P. Ring, *Phys. Rev. C* **78**, 034318 (2008).
- [53] Y. Tian, Z. Y. Ma, and P. Ring, *Phys. Lett. B* **676**, 44 (2009).
- [54] K. Nomura, N. Shimizu, and T. Otsuka, *Phys. Rev. Lett.* **101**, 142501 (2008).
- [55] K. Nomura, N. Shimizu, and T. Otsuka, *Phys. Rev. C* **81**, 044307 (2010).
- [56] K. Nomura, R. Rodríguez-Guzmán, L. M. Robledo, and N. Shimizu, *Phys. Rev. C* **86**, 034322 (2012).
- [57] K. Nomura, D. Vretenar, T. Nikšić, and B.-N. Lu, *Phys. Rev. C* **89**, 024312 (2014).
- [58] K. Nomura, T. Otsuka, N. Shimizu, and L. Guo, *Phys. Rev. C* **83**, 041302 (2011).
- [59] H. Schaaser and D. Brink, *Nucl. Phys. A* **452**, 1 (1986).
- [60] D. R. Inglis, *Phys. Rev.* **103**, 1786 (1956).
- [61] S. Beliaev, *Nucl. Phys.* **24**, 322 (1961).
- [62] Brookhaven National Nuclear Data Center, <http://www.nndc.bnl.gov>.
- [63] L. Wilets and M. Jean, *Phys. Rev.* **102**, 788 (1956).
- [64] J. J. Valiente-Dobón, T. Steinhardt, C. E. Svensson, A. V. Afanasjev, I. Ragnarsson, C. Andreoiu, R. A. E. Austin, M. P. Carpenter, D. Dashdorj, G. de Angelis, F. Döna, J. Eberth, E. Farnea, S. J. Freeman, A. Gadea, P. E. Garrett, A. Görge, G. F. Grinyer, B. Hyland, D. Jenkins, F. Johnston-Theasby, P. Joshi, A. Jungclauss, K. P. Lieb, A. O. Macchiavelli, E. F. Moore, G. Mukherjee, D. R. Napoli, A. A. Phillips, C. Plettner, W. Reviol, D. Sarantites, H. Schnare, M. A. Schumaker, R. Schwengner, D. Seweryniak, M. B. Smith, I. Stefanescu, O. Thelen, and R. Wadsworth, *Phys. Rev. Lett.* **95**, 232501 (2005).
- [65] C. Gross, J. Heese, K. Lieb, S. Ulbig, W. Nazarewicz, C. Lister, B. Varley, J. Billowes, A. Chishti, J. McNeill, and W. Gelletly, *Nucl. Phys. A* **501**, 367 (1989).
- [66] T. Kibédi and R. Spear, *At. Data and Nucl. Data Tables* **89**, 77 (2005).
- [67] N. Stone, *At. Data and Nucl. Data Tables* **90**, 75 (2005).
- [68] K. Nomura, R. Rodríguez-Guzmán, and L. M. Robledo, *Phys. Rev. C* **95**, 064310 (2017).